

**Search for Heavy Resonances Decaying to Tau Pairs with  
the CMS Experiment**

by

**A. A. Johnson**

B.S., Carnegie Mellon University, 2011

M.S., University of Colorado, 2013

A thesis submitted to the  
Faculty of the Graduate School of the  
University of Colorado in partial fulfillment  
of the requirements for the degree of  
Doctor of Philosophy  
Department of Physics  
2016

This thesis entitled:  
Search for Heavy Resonances Decaying to Tau Pairs with the CMS Experiment  
written by A. A. Johnson  
has been approved for the Department of Physics

---

Prof. John P. Cumalat

---

Prof. Kevin Stenson

---

Prof. Steven Wagner

Date \_\_\_\_\_

The final copy of this thesis has been examined by the signatories, and we find that both the content and the form meet acceptable presentation standards of scholarly work in the above mentioned discipline.

Johnson, A. A. (Ph.D., Physics)

Search for Heavy Resonances Decaying to Tau Pairs with the CMS Experiment

Thesis directed by Prof. John P. Cumalat

Two searches for heavy neutral resonances,  $Z\ell\ell$ s, decaying to back-to-back tau pairs are carried out using the Compact Muon Solenoid experiment at the Large Hadron Collider. The first, carried out during the 2012 data-taking run at  $\sqrt{s} = 8$  TeV, focuses on the fully-leptonic channel, in which one tau decays to an electron and the other to a muon. The second, carried out during the 2015 run at  $\sqrt{s} = 13$  TeV, focuses on the fully-hadronic channel, in which each tau decays to a hadronic jet. Each search employs a hybrid of background estimation strategies using both Monte Carlo simulation and data-driven methods. In both searches, observed data is found to be in agreement with Standard Model expectation and no excesses are observed. Limits are placed on the  $Z\ell\ell$ , culminating in a world-record limit of 2.2 TeV at 95% confidence level.

## **Dedication**

To my parents, Carl and Sharon Johnson. Without your constant love, support, and encouragement, none of this would have been remotely possible.

## Acknowledgements

Here's where you acknowledge folks who helped. But keep it short, i.e., no more than one page, as required by the Grad School Specifications.

## Contents

### Chapter

<b>1</b>	<b>Outline</b>	<b>1</b>
1.1	Standard model . . . . .	1
1.2	The CMS Experiment . . . . .	1
1.3	EMu channel @ 8TeV . . . . .	2
1.4	TauTau channel @ 13TeV . . . . .	2
<b>2</b>	<b>Introduction</b>	<b>3</b>
2.1	Introduction . . . . .	3
<b>3</b>	<b>The Compact Muon Solenoid (CMS) Experiment</b>	<b>5</b>
3.1	The silicon tracker . . . . .	6
3.1.1	The pixel detector . . . . .	7
3.1.2	The strip tracker . . . . .	9
3.2	The electromagnetic calorimeter . . . . .	9
3.3	The hadronic calorimeter . . . . .	10
3.4	The CMS magnet . . . . .	11
3.5	The muon system . . . . .	12
3.5.1	Drift tubes (DTs) . . . . .	13
3.5.2	Cathode strip chambers (CSCs) . . . . .	13
3.5.3	Resistive plate chambers (RPCs) . . . . .	14

3.6	The trigger system	14
3.6.1	The Level-1 (L1) trigger)	15
3.6.2	The High level trigger (HLT)	15
3.7	Particle Reconstruction	16
3.7.1	Particle Flow	16
<b>4</b>	Strategy	<b>22</b>
<b>5</b>	Triggers	<b>24</b>
5.0.1	Single Lepton Trigger Efficiency	25
5.0.2	Single Electron Trigger Efficiency	25
5.0.3	Single Muon Trigger Efficiency	26
5.0.4	Di-Tau Trigger Efficiency	26
<b>6</b>	Data and Monte Carlo Samples	<b>33</b>
6.1	Physics Object Reconstruction	34
6.2	Jet Reconstruction	34
<b>7</b>	Electron Reconstruction and Identification	<b>37</b>
<b>8</b>	Muon Reconstruction and Identification	<b>39</b>
<b>9</b>	Tau Reconstruction and Identification	<b>41</b>
9.0.1	Efficiency of Tau Identification discriminators	42
9.0.2	Tau Energy Scale and Resolution	44
9.1		
		45
<b>10</b>	Corrections for Pile-Up	<b>46</b>

<b>11</b>	Electron Reconstruction and Identification	<b>48</b>
<b>12</b>	Muon Reconstruction and Identification	<b>50</b>
<b>13</b>	Tau Reconstruction and Identification	<b>52</b>
13.0.1	Efficiency of Tau Identification discriminators . . . . .	53
13.0.2	Tau Energy Scale and Resolution . . . . .	55
13.1	Jet Reconstruction . . . . .	56
13.2	. . . . .	
	. . . . .	57
<b>14</b>	Muon + Hadronic Tau Channel	<b>59</b>
14.0.1	W + jets Background Estimation . . . . .	70
14.0.2	DY + jets Background Estimation . . . . .	78
14.0.3	Other Small Backgrounds . . . . .	82
<b>15</b>	The $\tau_h \tau_h$ Channel	<b>84</b>
15.0.1	QCD Background Estimation & Validation Strategy . . . . .	85
15.0.2	Background Estimation for $Z(\rightarrow \tau\tau) + \text{jets}$ . . . . .	91
<b>16</b>	Electron + Hadronic Tau Channel	<b>94</b>
16.0.1	Event selection . . . . .	94
16.0.2	Genuine dilepton events . . . . .	100
16.0.3	QCD multi-jet background . . . . .	101
16.0.4	W+jets background . . . . .	103
16.0.5	Overlays of observations and SM predictions . . . . .	110
16.0.6	Post-unblinding: further checks of the backgrounds . . . . .	110

<b>17</b>	Electron + Muon Channel	<b>117</b>
17.1	Event selection . . . . .	117
17.2	Genuine dilepton events . . . . .	118
17.2.1	Drell-Yan process . . . . .	118
17.2.2	$t\bar{t}$ and single top processes . . . . .	119
17.2.3	Di-boson process . . . . .	119
17.3	QCD multi-jet background . . . . .	119
17.4	W+jets background . . . . .	120
17.5	Overlays of observations and SM predictions . . . . .	120
<b>18</b>	Systematics	<b>130</b>
<b>19</b>	Results and Conclusions	<b>134</b>

## Appendix

## Tables

### **Table**

5.1	The trigger paths used to collected the data. Emulated trigger paths, in particular those most similar to the paths used to collect the data, are applied to the simulated samples.	24
5.2	Event rate in mu-tau control region after requiring denominator level selections	32
6.1	Collision Data Samples	33
6.2	MC Samples	36
6.3	Loose Jet-ID Selections.	36
7.1	Electron ID Selections.	38
8.1	$\mu$ Identification	40
9.1	Reconstructed Tau Decay Modes	41
11.1	Electron ID Selections.	49
12.1	$\mu$ Identification	51
13.1	Reconstructed Tau Decay Modes	52
13.2	Loose Jet-ID Selections.	57
14.1	Signal and background yields after various stages of the $\mu\tau_h$ selection.	70

14.2 Background and data yields in W + jets control regions $A, B, C$ , under nominal <i>conditions (i.e.</i>	
$\ell \not\in 30GeV)$ . . . . .	77
14.3 Background and data yields in W + jets control regions $A, B, C$ obtained without a <i>requirement.</i>	
. . . . .	78
14.4 Events in the W + jets high $m_T(\mu, \nu)$ control region for data and MC. . . . .	80
14.5 Events in the $Z \rightarrow \tau\tau$ control region for data and MC. . . . .	82
14.6 Yields in the $\mu\tau_h$ QCD control region for data and MC. . . . .	83
15.1 Yields in the controls region 1(B) and 1(D) used for calculation of OS/LS ratio. . . . .	88
15.2 Background and data yields in QCD control regions $A$ and $C$ under nominal isolation and <i>conditions (i.e. isolated</i>	
$+ \ell \not\in 30GeV)$ . . . . .	91
15.3 QCD yields in the isolated regions $A$ (signal region), $B$ , $C$ , and $D$ . . . . .	91
18.1 Summary of systematic uncertainties. Values are given in percent. “s” indicates template variations (“shape” uncertainties). . . . .	133
19.1 Event summary table after signal region selection . . . . .	137

## Figures

### **Figure**

3.1	The Large Hadron Collider located underneath the Franco-Swiss border at CERN near Geneva, Switzerland. The CMS Experiment is located on the French side in Cessy, France . . . . .	5
3.2	The CMS Experiment (open for maintenance) . . . . .	6
3.3	Schematic of the CMS Experiment showing the silicon trackers, electromagnetic calorimeter (ECAL), hadronic calorimeter (HCAL), superconducting solenoid, steel return yoke, and muon system. . . . .	7
3.4	Overview of the silicon tracker layout. . . . .	8
3.5	Diagram indicating the layout of the barrel pixel (BPIX) sensors (in green) and endcap pixel (FPIX) sensors (in pink) . . . . .	8
3.6	Layout of the electromagnetic calorimeter (ECAL) indicating the configuration of the barrel (EB) and endcap (EE) crystals. . . . .	10
3.7	Layout of the hadronic calorimeter (HCAL) indicating the configuration of the barrel (HB) and endcap (HE) components as well as the outer HCAL (HO) lining the solenoid. . . . .	11
3.8	The superconducting solenoid. . . . .	12
3.9	Layout of the muon system highlighting the layered structure of the drift tubes (DTs, green), cathode strip chambers (CSCs, blue), and resistive plate chambers (RPCs, red). . . . .	13

5.1	The efficiency vs. curves of the single-electron triggers used. Left column: barrel. Right column: endcap. The offline electron ID requirements used are HEEP (top row), MVANonTrig80 (middle row), MVATrigWP80 (bottom row). . . . .	27
5.2	The efficiency vs. curves of the single-electron triggers used. Left column: barrel. Right column: endcap. The offline electron ID requirements used are HEEP (top row), MVANonTrig80 (middle row), MVATrigWP80 (bottom row). The two bins each contain half of the events with $> 35$ . . . . .	28
5.3	The efficiency vs. curves of the single-muon triggers used. Left column: $ \eta  < 1.2$ . Right column: $ \eta  > 1.2$ . Bottom row: the two bins each contain half of the events with $> 25$ . . . . .	29
5.4	The per-leg $\tau_h$ trigger efficiency as a function of $p_T(\tau_h)$ for (a) simulated $Z'$ signal sample on left (b) for data and all backgrounds obtained by requiring mu-tau region on right. . . . .	31
9.1	Decay Mode Finding efficiency as function of $p_T$ , $\eta$ , and number of vertices of generator-level taus . . . . .	43
9.2	Efficiency of anti-muon discriminator (Loose3) as function of $p_T$ , $\eta$ , and number of vertices of generator-level taus . . . . .	43
9.3	Efficiency of anti-electron discriminator (Loose/Medium MVA5) as function of $p_T$ , $\eta$ , and number of vertices of generator-level taus . . . . .	44
9.4	Efficiency of isolation discriminator ("CombinedIsoDB3Hits") as function of $p_T$ , $\eta$ , and number of vertices of generator-level taus . . . . .	44
9.5	Energy response of reconstructed taus, raw and vs. generated tau $p_T$ . . . . .	45

10.1 Distributions of the number of reconstructed primary vertices. Top: $e\mu$ channel. Bottom: $e\tau_h$ channel. Left: before reweighting. Right: after reweighting (“official” 69 mb). The ratios after reweighting become flattest at an “unofficial” value of 71 mb. The apparent substantial differences in the QCD “integrals” are artifacts of the plotting procedure, in which bins with negative contributions are zero-ed. . . . .	47
13.1 Decay Mode Finding efficiency as function of $p_T$ , $\eta$ , and number of vertices of generator-level taus . . . . .	54
13.2 Efficiency of anti-muon discriminator (Loose3) as function of $p_T$ , $\eta$ , and number of vertices of generator-level taus . . . . .	54
13.3 Efficiency of anti-electron discriminator (Loose/Medium MVA5) as function of $p_T$ , $\eta$ , and number of vertices of generator-level taus . . . . .	55
13.4 Efficiency of isolation discriminator (“CombinedIsoDB3Hits”) as function of $p_T$ , $\eta$ , and number of vertices of generator-level taus . . . . .	55
13.5 Energy response of reconstructed taus, raw and vs. generated tau $p_T$ . . . . .	56
14.1 Left: $p_T(\mu)$ after acceptance, $\mu$ identification, and $\tau_h$ identification cuts. Right: $p_T(\tau_h)$ after acceptance, $\mu$ identification, and $\tau_h$ identification cuts. . . . .	60
14.2 Left:  <i>after acceptance,</i>	
$\mu$ identification, and $\tau_h$ identification cuts. Right: $P_\zeta - 3.1 \times P_\zeta^{vis}$ after acceptance, $\mu$ identification, and $\tau_h$ identification cuts. . . . .	61
14.3 Sketch depicting the W+jets rejection power of a $\Delta\phi$ cut. . . . .	62
14.4 Definitions for $p_\zeta$ and $p_\zeta^{vis}$ . . . . .	64
14.5 $p_\zeta p_\zeta^{vis}$ for $Z' \rightarrow \tau\tau$ . . . . .	65
14.6 $p_\zeta p_\zeta^{vis}$ for W+Jets. . . . .	66
14.7 Left: $\cos\Delta\phi$ between the muon and tau/jet directions. Right: $m(\mu, \tau_h,)$ for signal $Z'$ and various backgrounds. . . . .	69

14.8 $p_T(\tau_h)$ ,	$\eta(\tau_h)$ ,	
	, and	
$m_T(\mu,)$ control plots using events satisfying the “preselection” requirements. The background predictions are entirely based on MC. . . . .	71	
14.9 $p_T(\tau_h)$ ,	$\eta(\tau_h)$ ,	
	, and	
$m_T(\mu,)$ control plots using events satisfying the signal region requirements. The background predictions are entirely based on MC. . . . .	72	
14.10 Left: Comparison of the $\zeta$ distribution in $W + \text{jets}$ MC, normalized to unity, for events with isolated and non-isolated $\tau_h$ . Right: Comparison of the $\cos\Delta\phi$ distribution in $W + \text{jets}$ MC, normalized to unity, for events with isolated and non-isolated $\tau_h$ . . . . .	74	
14.11 Top Left: $W + \text{jets}$ closure test performed with simulation (normal scale to focus on low mass) . . . . .	under nominal conditions( <i>i.e.</i>	
$\zeta \sim 30\text{GeV}$ ).TopRight : $W + \text{jets}$ closure test performed with simulation ( <i>log scale to focus on the high mass tail</i> ) $\sim 30\text{GeV}$ ).MiddleLeft : $W + \text{jets}$ closure test performed with simulation ( <i>normal scale to focus on low mass</i> ), $\sim 0\text{GeV}$ .MiddleRight : $W + \text{jets}$ closure test performed with simulation ( <i>log scale to focus on the high mass tails</i> ) $\sim 0\text{GeV}$ .BottomLeft : Comparison of the reconstructed mass distributions in regions A and B, in normal scale . . . . .	75	
14.12 Top Left: $m_T(\mu,)$ distributions in $W + \text{jets}$ control region C, under nominal conditions( <i>i.e.</i>		
$\zeta \sim 30\text{GeV}$ ).TopRight : $m_T(\mu,)$ distributions in $W + \text{jets}$ control region A, under nominal conditions( <i>i.e.</i>		

$\zeta < 30\text{GeV}).$ Bottom Left : $m_T(\mu, \tau_h)$ distributions in $W + \text{jets}$ control region $C$ , requiring $> 0$ GeV. Bottom Right: $m_T(\mu, \tau_h)$ distributions in $W + \text{jets}$ control region $A$ , requiring $> 0$ GeV. . . . .	76
14.13 $p_T(\tau_h)$ and $\eta(\tau_h)$ distributions in the $W + \text{jets}$ high $m_T(\mu, \tau_h)$ control region. . . . .	79
14.14 $m(\mu, \tau_h, \tau_h)$ distribution in the $Z \rightarrow \tau\tau$ control region defined by $< 30$ GeV and $m(\mu, \tau_h, \tau_h) < 300$ GeV, with otherwise similar selections to the signal region. . . . .	81
15.1 QCD estimation and validation strategy for the $\tau_h\tau_h$ channel. . . . .	87
15.2 $\tau_h - \tau_h$ mass distribution in isolated OS, low- <i>sideband(Left : normalscale.Right : logscale).</i>	89
15.3 $m(\tau_h, \tau_h)$ mass distribution in anti-isolated OS, low- <i>sideband(Left : normalscale.Right : logscale).</i>	89
15.4 $m(\tau_h, \tau_h)$ mass distribution in anti-isolated OS region with nominal <i>(Left : normalscale.Right : logscale).</i>	90
15.5 $m(\tau_h\tau_h)$ in the $Z \rightarrow \tau\tau$ control region obtained using the “pre-selection” cuts, and additionally requiring $\tau_h\tau_h$ pairs with invariant mass less than 100 GeV. . . . .	93
16.1 Distributions, after preselection, of the variables used for signal selection: (top left), “ $\zeta$ ” (top right), $\cos \Delta\phi(e, \tau_h)$ (bottom left), and $n_b$ (bottom right). . . . .	96
16.2 Distributions, after preselection, of electron (top left), electron pseudo-rapidity (top right), $\tau$ (bottom left), $\tau$ pseudo-rapidity (bottom right). . . . .	97
16.3 Distributions, after preselection, of $m_T(e, \tau_h)$ (left), $m(e, \tau_h, \tau_h)$ (right). . . . .	98

16.4 Distributions of the variables used for signal selection, after all other signal selection requirements on variables other than the one plotted: (top left), “ $\zeta$ ” (top right), $\cos \Delta\phi(e, \tau_h)$ (bottom left), and $n_b$ (bottom right). . . . .	99
16.5 Distributions of . Left: validation region with $< 30$ , $n_b = 0 < 200$ GeV. Right: validation region with $n_b \geq 1$ . . . . .	102
16.6 QCD estimation and validation strategy for the channel. . . . .	102
16.7 channel: scan of the range of relaxed isolation for the $\tau_h$ . Left: text within each bin gives the normalization factor applied to same-charge iso-relaxed events (“loose to tight” factor); the color axis matches the right plot. Right: $\chi^2$ -probability of the agreement between the predicted and observed distributions of tightly-isolated same-charge events. . . . .	104
16.8 The distribution of reconstructed parent mass, , in the same-charge, tightly-isolated sample: channel. . . . .	105
16.9 Left: comparison of the simulated distributions of , using tight $\tau_h$ isolation and with relaxed $\tau_h$ isolation, in the control region described in Section 16.0.4. Center: analogous comparison for the signal region. Right: comparison in the signal region of the “tighter” and “looser” halves of the sideband. . . . .	107
16.10 Distributions of $m_T(e, )$ obtained in the W-enriched control region, when scanning the W+jets event rate from 1.0 to 1.25 times its nominal value, in steps of 0.05. For each assumed W+jets event rate, the QCD prediction is determined anew using the procedure described in Section 16.0.3. . . . .	108
16.11 channel: the distribution of reconstructed parent mass, , in the W-validation region described in Section 16.0.4. . . . .	109
16.12 Left: predicted background yields and observed event yields in the channel after signal selection. Right: the distribution of transverse mass. . . . .	111
16.13 Distributions, after final selection, of electron (top left), electron pseudo-rapidity (top right), $\tau$ (bottom left), $\tau$ pseudo-rapidity (bottom right). . . . .	112

16.14channel, in the signal region, requiring also $60 \text{ GeV} < m_T < 120 \text{ GeV}$ . Left: The distributions of with W+Jets shape estimated from relaxed $\tau_h$ isolation region. Right: The distributions of with W+Jets shape estimated from tight $\tau_h$ isolation region. . . . .	113
16.15In the signal region, but requiring 2-prong $\tau_h$ 's: the distribution of reconstructed parent mass, , with W+Jets shape estimated from relaxed $\tau_h$ isolation region. . . . .	114
16.16Left: W+jets shape and yield from simulation Right: Data-driven W+jets estimation channel: . . . . .	116
17.1 Distributions, after preselection, of the variables used for the signal selection: (top left), “ $\zeta$ ” (top right), $\cos \Delta\phi(e, \mu)$ (bottom left), and $n_b$ (bottom right). . . . .	121
17.2 Distributions, after preselection, of electron (top left), electron pseudo-rapidity (top right), muon (bottom left), muon pseudo-rapidity (bottom right). . . . .	122
17.3 Distributions, after preselection, of $m(e, \mu, )$ (top), $m_T(e, )$ (bottom left), and $m_T(\mu, )$ (bottom right). . . . .	123
17.4 Distributions of the variables used for signal selection, after all other signal selection requirements on variables other than the one plotted: (top left), “ $\zeta$ ” (top right), $\cos \Delta\phi(e, \mu)$ (bottom left), and $n_b$ (bottom right). . . . .	124
17.5 Distributions of . Left: validation region with $< 30$ , $n_b = 0$ and $< 125 \text{ GeV}$ . Right: validation region with $> 30$ , $n_b \geq 1$ and $P_\zeta - 3.1 \times P_\zeta^{vis} > -50$ . . . . .	125
17.6 channel: scan of the range of relaxed relative isolation for the muon. Left: text within each bin gives the normalization factor applied to same-charge iso-relaxed events (“loose to tight” factor); the color axis matches the right plot. Right: $\chi^2$ of the agreement between the predicted and observed distributions of tightly-isolated same-charge events. . . . .	126
17.7 The distribution of reconstructed parent mass, , in the same-charge, tightly-isolated sample: channel. . . . .	127

17.8 Top: predicted background yields and observed event yields in the channel after signal selection. Bottom: distributions of transverse mass. . . . .	128
17.9 Distributions, after final selection, of electron (top left), electron pseudo-rapidity (top right), muon (bottom left), muon pseudo-rapidity (bottom right). . . . .	129
19.1 Top Left: $m(\mu, \tau_h, )$ distribution in the signal region, in log scale. Top Right: $m(\tau_h, \tau_h, )$ distribution in the signal region, in log scale. Bottom Left: $m(e, \tau_h, )$ distribution in the signal region, in log scale. Bottom Right: $m(e, \mu, )$ distribution in the signal region, in log scale. . . . .	136
19.2 Expected and observed limits for the $\tau_\mu\tau_h$ , $\tau_h\tau_h$ , $\tau_e\tau_h$ , $\tau_e\tau_\mu$ channels. A k factor of 1.3 has been used to scale the leading order (LO) signal cross-section. . . . .	138
19.3 Combined expected limit for the $\tau_\mu\tau_h$ , $\tau_h\tau_h$ , $\tau_e\tau_h$ , $\tau_e\tau_\mu$ channels. . . . .	139
19.4 Combined expected limit for the $\tau_\mu\tau_h$ , $\tau_h\tau_h$ , $\tau_e\tau_h$ , $\tau_e\tau_\mu$ channels. A k factor of 1.3 has been used to scale the leading order (LO) signal cross-section. . . . .	139

## **Chapter 1**

### **Outline**

#### **OUTLINE**

##### **1.1 Standard model**

Z'

Why TauTau

Other BSM theories involving ditau pairs

##### **1.2 The CMS Experiment**

Pixels

Monitoring tool

Strips

ECAL

HCAL

Muon System

Triggering

L1 HLT

Computing @ CERN

### **1.3 EMu channel @ 8TeV**

MC samples used  
Generation methods  
Data samples used  
Object selection  
Validation  
Background estimation  
Lifetime cuts optimization  
Systematics  
Limit setting methodology impact of lifetime cuts on limit

### **1.4 TauTau channel @ 13TeV**

MC samples used  
Generation methods  
Data samples used  
Object selection  
Validation  
Background estimation  
Lifetime cuts optimization  
Systematics  
Limit setting methodology impact of lifetime cuts on limit

## Chapter 2

### Introduction

#### 2.1 Introduction

At the forefront of the interconnection between particle physics and cosmology are the following questions: (1) What is the origin of the matter-antimatter asymmetry?; (2) What is the origin of neutrino mass?; (3) Are there new fundamental forces in nature?; (4) What is the origin of dark energy; and (5) Is the Higgs boson solely responsible for electroweak symmetry breaking and the origin of mass? Much like the Higgs mechanism is introduced to account for the  $SU(2)\times U(1)$  symmetry breaking, there are a plethora of theoretical models which incorporate additional gauge fields and interactions to address these questions. For example, string theory is considered a promising candidate for describing gravitational systems at strong coupling and thus plays a prominent role in the description of black holes and evolution of the universe through the understanding of the origin of dark energy. Similarly, models with additional neutrino fields at the TeV scale provide a possible explanation for the mass of light neutrinos. Such models often manifest themselves as new heavy particles that could be observed at the LHC. Surprisingly, some of these new particles predicted on the basis of pure particle physics arguments can even provide the correct dark matter relic density. There are several ways new heavy gauge bosons appear. The most natural possibility is one in which these heavy gauge bosons are the gauge field of a new local broken symmetry. Examples include models with a new  $U(1)$  gauge symmetry, little Higgs models, and E6 Grand Unified Theories (GUT). In models with a new  $U(1)$  gauge symmetry, the  $Z'$  is the gauge boson of the broken symmetry. In little Higgs models, breaking of the global symmetry by gauge and

Yukawa interactions generates Higgs mass and couplings at the TeV scale that cancel off the SM quadratic divergence of the Higgs mass from top, gauge, and Higgs loops. This results in one or more  $Z'$  bosons. In Kaluza-Klein models, the  $Z'$  bosons are excited states of a neutral, bulk gauge symmetry. From the breadth, scope, and implications of these models, it is apparent that probing these questions and puzzles potentially lies in the physics of new particles at the TeV scale.

Of particular interest for this analysis are models that include an extra neutral gauge boson that decays to pairs of high- $p_T \tau$  leptons. Although many models with extra gauge bosons obey the universality of the couplings, some models include generational dependent couplings resulting in extra neutral gauge bosons that preferentially decay to  $\tau$  leptons, making this analysis an important mode for discovery. However, even if a new gauge boson decaying to  $\mu\mu$  is discovered first, it will be critical to establish the  $\tau\tau$  decay channel to establish the coupling relative to  $\mu\mu$  channel.

## Chapter 3

### The Compact Muon Solenoid (CMS) Experiment

The CMS Experiment is a multipurpose particle detector located on the LHC ring underneath the Franco-Swiss border at CERN in Geneva, Switzerland. An overview of the experiments on the LHC ring can be seen in Figure 3.1. The experiment is located 100 meters underground in Cessy, France. CMS is 28.7 meters long, 15.0 meters in diameter, and weighs approximately 14,000 tonnes. It's arranged in a cylindrical, multi-layered structure consisting of a "barrel" and two endcaps, with the LHC beam passing through the vertical axis of the cylinder. CMS consists of several subdetectors, each designed to measure a different class or property of particle. From the beam line outward, the layers of CMS are the tracker, the electromagnetic calorimeter (ECAL), the hadronic calorimeter (HCAL), the superconducting solenoid, and the muon system (interspersed with the steel return yoke). A photograph of CMS can be seen in Figure 3.2.



Figure 3.1: The Large Hadron Collider located underneath the Franco-Swiss border at CERN near Geneva, Switzerland. The CMS Experiment is located on the French side in Cessy, France

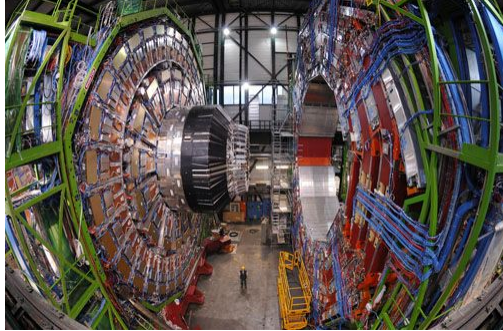


Figure 3.2: The CMS Experiment (open for maintenance)

The experiment uses a right-handed coordinate system: the origin is set at the  $pp$  collision point, with the  $x$ -axis pointing towards the center of the LHC ring, the  $y$ -axis pointing straight up, and the  $z$ -axis pointing along the beam line in the counter-clockwise direction. CMS also uses a pseudo-polar coordinate system, with  $\theta$  defined as the polar angle from the beam axis, and  $\eta$  as the "pseudorapidity", itself defined as

$$\eta = -\ln [\tan (\theta/2)] \quad (3.1)$$

A diagram highlighting the layout of CMS can be seen in Figure 3.3.

### 3.1 The silicon tracker

The silicon tracker is the innermost detector element in CMS, and is designed to offer the highest resolution measurement of charged particle trajectories (such trajectories are referred to as "tracks"). The tracker is composed of approximately  $200\text{m}^2$  of silicon, and includes arrays of silicon pixels in the inner layer and arrays of silicon strips in the outer layer. The silicon elements are arranged in the densest configuration near to the interaction vertex ( $r \approx 10\text{cm}$ ), with pixel size  $\approx 100 \times 150\mu\text{m}^2$ . As one moves away from the interaction vertex, the solid angle becomes large enough that the particle flux drops off to a degree that larger silicon elements may be used

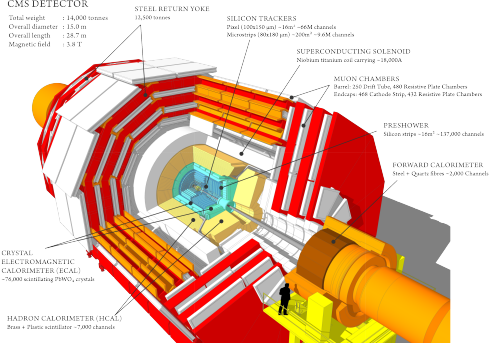


Figure 3.3: Schematic of the CMS Experiment showing the silicon trackers, electromagnetic calorimeter (ECAL), hadronic calorimeter (HCAL), superconducting solenoid, steel return yoke, and muon system.

(silicon strips measuring  $10\text{cm} \times 80\mu\text{m}$  at  $20\text{cm}r55\text{cm}$ , silicon strips measuring  $25\text{cm} \times 180\mu\text{m}$  for  $r55\text{cm}$ . The total number of silicon elements is 66 million pixels and 9.6 million strips. The tracker is divided into a barrel segment and two forward endcaps. The endcaps contain two pixel and nine strip layers each, and the barrel segment is separated into an inner and outer barrel. A schematic of the tracker layout can be seen in Figure 3.4. Particle tracks are reconstructed from hits in the individual silicon pixels/strips, the track being interpolated between hits.

### 3.1.1 The pixel detector

The pixel detector, shown in Figure fig(PixelLayout), consists of three barrel layers and two endcap layers. The barrel has a length of 53 cm, and the endcap disks range from 6 cm to 15 cm in radius. The pixel modules are arranged in a ladder-like configuration in the barrel, with 768 total modules comprising the barrel. The endcap disks are arranged in a turbine-like fashion, with 24 "blades" per disk, and 7 pixel modules per blade for a total of 672 pixel modules in the endcaps. Each pixel consists of a readout chip (ROC), which are bump bonded to the modules. In total, the pixel detector includes about 16,000 ROCs.

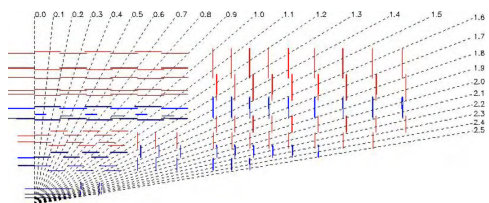


Figure 3.4: Overview of the silicon tracker layout.

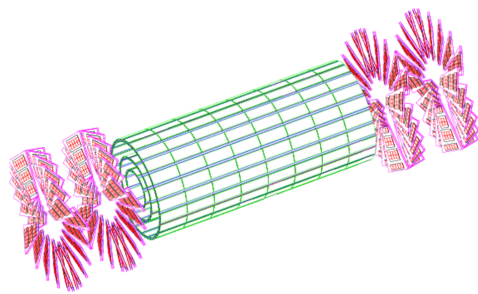


Figure 3.5: Diagram indicating the layout of the barrel pixel (BPIX) sensors (in green) and endcap pixel (FPIX) sensors (in pink)

### 3.1.2 The strip tracker

The strip tracker is divided into a barrel segment and two endcap segments. The barrel segment is itself divided into a Tracker Inner Barrel (TIB) section and a Tracker Outer Barrel (TOB) section. The TIB includes four layers of silicon strips each  $320\mu\text{m}$  thick and ranging in pitch from  $80\mu\text{m}$  and  $120\mu\text{m}$ . In the TOB, the lower rate of particle flux allows for larger strips (each  $500\mu\text{m}$  thick and ranging in pitch from  $120\mu\text{m}$  to  $180\mu\text{m}$ ).

The endcaps are each comprised of a Tracker Endcap (TEC) and Tracker Inner Disks (TIDs). The TIDs are designed to fill the region between the TEC and the TIB. The TECs each contain nine disks, and each TID contains three disks. On each disk, the modules (for both TID and TEC) are arranged in rings centered on the beam line. The TID strips (and three innermost ring strips of the TEC) have thickness  $320\mu\text{m}$ , while the rest of the TEC strips have thickness  $500\mu\text{m}$ . In total the strip tracker contains about 15,400 strip modules.

## 3.2 The electromagnetic calorimeter

The next layer outward from the silicon tracker is the electromagnetic calorimeter (ECAL), which is designed primarily to measure energies of photons and electrons. The ECAL consists of an array of about 75,000 lead tungstate ( $\text{PbWO}_4$ ) crystals, and has a barrel (BE) segment as well as two endcap (EE) segments. The BE segment has 61,200 crystals, while each EE segment contains 7,324 crystals.

$\text{PbWO}_4$  was chosen for the ECAL due to its short radiation length ( $X_0 = 0.89\text{ cm}$ ), fast response time (80% of light emitted within 25ns), and radiation hardness (up to 10 Mrad).

The barrel (EB) crystals present an apparent cross-section (when viewed from the interaction vertex) of  $\approx 22 \times 22\text{ mm}^2$ , and are 230 mm (25.8 radiation lengths) thick. The barrel has an inner radius of 129 cm, and covers the pseudorapidity range  $0|\eta|1.479$ .

The endcap (EE) crystals are each arranged in two D-shaped semicircular aluminum plates. From these plates are cantilevered "supercrystal" structures consisting of 5x5 crystal blocks. Each

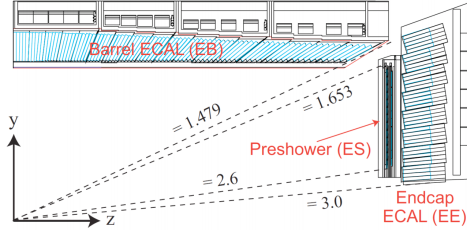


Figure 3.6: Layout of the electromagnetic calorimeter (ECAL) indicating the configuration of the barrel (EB) and endcap (EE) crystals.

crystal presents an apparent cross-section of  $\approx 28.6 \times 28.6 \text{ mm}^2$ , and are 220 mm (24.7 radiation lengths) thick, and the endcap crystals cover the pseudorapidity range  $1.479|\eta|3.0$ .

A diagram of the ECAL layout can be seen in Figure 3.6.

### 3.3 The hadronic calorimeter

Surrounding the ECAL is the hadronic calorimeter (HCAL). The primary function of the HCAL is to measure the energies of hadrons (particles made of quarks and gluons). Located just inside the solenoid magnet, the HCAL is primarily composed of brass panels made from melted-down artillery shells. Interspersed with the brass panels are plastic scintillation panels, in which are embedded wavelength-shifting (WLS) fibers, which carry the signal to clear fibers outside the scintillators for readout. As hadrons enter the HCAL, they produce secondary particles in the brass which in turn create further particles. These hadron "showers" then interact with the plastic scintillators, where the fibers carry the signal to hybrid photodiodes so the signal can be measured.

HCAL is divided into barrel (HB) and endcap (HE) portions. Due to limited space between the ECAL and solenoid, the HCAL also includes material outside the solenoid: the outer HCAL (HO) lining the solenoid, and the forward calorimeter (HF) outside the muon endcap system. These additions increase the total radiation lengths covered by the HCAL to 10.

While HB and HE use the brass-plastic configuration, HO uses the solenoid itself instead of the brass, although the same plastic scintillators are used. The HF uses steel in place of brass, and quartz fibers in place of plastic scintillators. This is done to preferentially select neutral

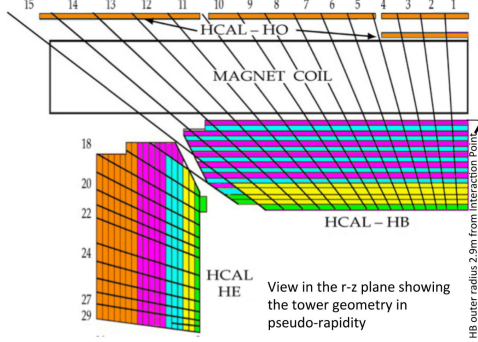


Figure 3.7: Layout of the hadronic calorimeter (HCAL) indicating the configuration of the barrel (HB) and endcap (HE) components as well as the outer HCAL (HO) lining the solenoid.

components of hadron showers, which are shorter and narrower and are thus well suited for the forward environment, which tends to be quite congested with particles.

A diagram of the HCAL layout is shown in Figure *fig(HCAL<sub>Layout</sub>)*.

### 3.4 The CMS magnet

The need to measure high  $p_T$  muons has driven the requirements on the CMS magnetic field strength. With the goal to accurately determine both momentum and sign of 1TeV muons at  $/p \approx 10\%$ , a superconducting solenoid with an interior magnetic field strength of 3.8T was chosen as the central design feature of CMS.

The solenoid is located outside the silicon tracker, ECAL, and HCAL systems but inside the muon system. Interspersed with the muon system is the steel return yoke, which contains the field outside the solenoid and provides a 2T field to allow the muon system to measure charged particle momentum.

To generate the magnetic field, 18,160 amperes are passed through four layers of tightly-wound superconducting Nb-Ti wire, resulting in a stored energy of 2.3 gigajoules.

The magnetic field generated by the solenoid bends charged particles according to the equation

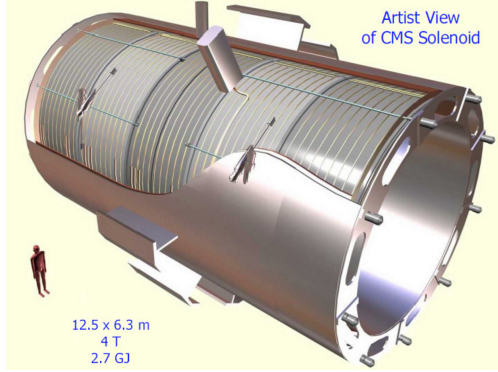


Figure 3.8: The superconducting solenoid.

$$R = p_T \frac{1}{0.3eB}$$

(3.2)

where  $R$  is the radius of curvature (in meters),  $p_T$  is the transverse momentum (in GeV),  $e$  is the electron charge (in Coulombs), and  $B$  is the field strength (in Tesla). Thus, the transverse momentum ( $p_T$ ) of the charged particle can be measured from the known field strength and the observed radius of curvature of the tracks measured in the tracker and muon systems.

An artist's rendition of the superconducting solenoid can be seen in Figure 3.8.

### 3.5 The muon system

The muon system is the outermost subdetector, and is central to the design of CMS. It is composed of three separate sensor elements: drift tubes (DTs), cathode strip chambers (CSCs), and resistive plate chambers (RPCs). A diagram of one quadrant of the muon system can be seen in Figure fig(muonSystemLayout). "MB" indicates the muon barrel subdetector, which is composed of DTs, "RB" indicates the RPC barrel subdetector, "ME" indicates the muon endcap subdetector (CSCs), and "RE" indicates the RPC endcap subdetector.

An overview of the layout of the muon system can be seen in Figure 3.9

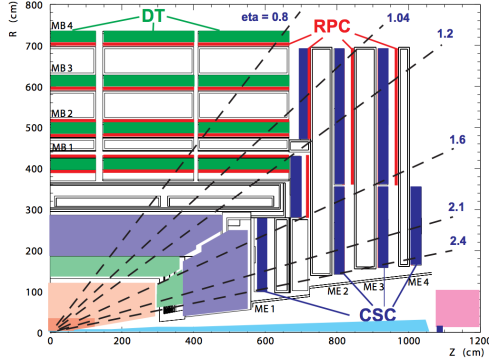


Figure 3.9: Layout of the muon system highlighting the layered structure of the drift tubes (DTs, green), cathode strip chambers (CSCs, blue), and resistive plate chambers (RPCs, red).

### 3.5.1 Drift tubes (DTs)

The barrel of the muon system contains 250 layers of DTs arranged in four layers (labeled MB1, MB2, MB3, and MB4 in Figure fig(muonSystemLayout)). In the MB1, MB2, and MB3 layers, DTs are arranged in 8  $r - \phi$ -measuring planes, and 4  $z$ -measuring planes. The MB4 layer only contains  $r - \phi$ -measuring planes.

Each DT is filled with a gaseous mixture of Argon ( 85%) and carbon dioxide ( 15%). Charged particles passing through the DT will ionize the gaseous mixture and produce a current along a central filament to be read out. The maximum drift length per DT is 2.0cm and the single point resolution is  $\approx 200 \mu\text{m}$ .

### 3.5.2 Cathode strip chambers (CSCs)

The muon endcap (ME) system is comprised of 234 CSCs in each endcap. The CSCs are trapezoidal in shape and are arranged in four layers (labeled ME1, ME2, ME3, and ME4 in Figure fig(muonSystemLayout)). The innermost layer (ME1), is made of 108 CSCs arranged in three rings of 36 CSCs each. The other layers each have two rings (18 CSCs on the inner ring, 36 on the outer ring, for a total of 54 CSCs per layer).

Each CSC is comprised of six gas gaps, with each gap containing a radial array of cathode strips and a plane of anode wires running perpendicular to the cathodes. The CSCs are overlapped

in  $\phi$  to avoid gaps in the particle acceptance. When a charged particle ionizes the gas, it leaves a charge on the anode wire and an image charge on a group of cathode strips. The spatial resolution provided from each CSC is  $\approx 200\mu\text{m}$ .

The forward (endcap) region of the muon system can expect a higher muon flux, so CSCs were chosen due to their fast response time and fine resolution.

### 3.5.3 Resistive plate chambers (RPCs)

RPCs can be found in both the barrel and endcaps of the muon system, and are used in parallel with the other two subsystems. The RPCs have timing resolution on the order of nanoseconds and are used primarily to resolve ambiguities in cases of multiple hits in the DTs or CSCs, thereby improving the overall accuracy of particle reconstruction.

There are two layers of RPCs "sandwiching" each of the first two DT layers (MB1 and MB2), while the outer DT layers (MB3 and MB4) are paired with one RPC each. The endcap CSCs are also paired with one RPC each.

Each RPC is comprised of parallel plates of bakelite enclosing two millimeter-thick gas gaps. Each gas gap contains a mixture of 96.2% R134a ( $\text{C}_2\text{H}_2\text{F}_4$ ), 3.5% isobutane ( $\text{C}_4\text{H}_{10}$ ), and 0.3% sulfur hexafluoride ( $\text{SF}_6$ ).

## 3.6 The trigger system

When running at full luminosity, the LHC generates  $pp$  collisions at a rate of 40MHz. With each event requiring  $\approx 10\text{MB}$  of digital storage space, this equates to a data-generation rate of 400TB per second. Since this is obviously unsustainable with current computer storage technology, CMS employs a trigger system to reduce the rate of stored events. Two levels of triggering are used: the hardware-based Level-1 (L1) trigger, which reduces the rate from 40MHz to approximately 100kHz, and the hardware-and-software-based High Level Trigger (HLT), which reduces the rate from  $\approx 100\text{kHz}$  to 300Hz.

### 3.6.1 The Level-1 (L1) trigger)

The L1 trigger takes data from the muon system, HCAL, and ECAL in order to make a rapid decision about whether or not to keep the event and send it to the HLT for further review. The L1 triggering rate is about  $3.2\mu\text{s}$ , during which time the entirety of the data from the event is temporarily stored. Information from the silicon tracker is not used in this stage of triggering, as the time required by the tracker to reconstruct a track is outside this triggering time window.

The L1 trigger is divided into three major components: the calorimeter trigger, the muon trigger, and the global trigger. The calorimeter trigger looks at the combined (summed) energy deposits in ECAL and HCAL. If the sum is greater than a given threshold, an "accept" signal is sent to the global trigger. The muon trigger looks at the DTs, CSCs, and RPCs which in conjunction form the muon system. If they in concert report at least four muons, each having high transverse momentum and high-resolution tracks ("good"-quality muons), an "accept" signal is sent to the global trigger. The global trigger makes the final decision to reject the event or, if it has received "accept" signals from both the calorimeter trigger and muon trigger, to send it to the HLT.

### 3.6.2 The High level trigger (HLT)

The HLT is software-based and uses software-defined "HLT paths" in order to determine whether or not a given event will pass a particular physics object selection determined by the path. The advantage of this setup is that different HLT paths can be used by different analysis groups looking for different physics signatures.

The HLT first reconstructs the entirety of the event from the stored data passed to it by the L1 trigger, and determines whether the event passes a given trigger path. There are four broad categories of HLT path: electrons/photons and muons, jets, missing transverse energy ( $\cancel{E}_T$ ), and taus. Hundreds of specific paths offering high levels of discrimination between required selection criteria are available and grouped into these four categories. As the paths are software-based and not hardware-based, new paths can be customized to the needs of any analysis effort.

In order to determine whether or not an event passes a given path, the entire event is reconstructed and run through three broad triggering steps: Stage 2 (calorimetry), Stage 2.5 (calorimetry+pixel hits), and Stage 3 (full reconstruction). In Stage 2, a threshold on calorimeter energy is applied. An object must have a combined ECAL+HCAL calorimetry energy greater than the threshold specified by the path in order to move on to Stage 2.5. In Stage 2.5, information from the pixel subdetector in the silicon tracker is used in order to verify that the hits recorded in the calorimetry towers have corresponding tracks in the pixel system (assuming the particle in question is charged). Finally, in Stage 3, information from the entire detector is used to reconstruct the entirety of objects in the event and ensure that they pass momentum, energy, and quality criteria specified by the path.

### **3.7 Particle Reconstruction**

Even after a given event has passed the L1 trigger and HLT requirements, its constituent particles only exist as hit patterns in the various subdetectors of CMS. In order for any kind of meaningful physics analysis to be performed, these hit patterns must be turned into physics objects which are more easily-read by the CMS software framework (CMSSW). Broadly, the six principle objects that are "reconstructed" from raw detector data in this manner are: electrons, muons, taus, photons, jets, and missing energy (). The chief set of software tools used to reconstruct physics objects is a group of algorithms collectively referred to as Particle Flow (PF).

#### **3.7.1 Particle Flow**

Particle Flow (PF) is the term used to refer to the general set of algorithms used to reconstruct physics objects (particles) out of raw detector data. The fundamental inputs to the PF algorithms are the charged particle tracks (from the silicon tracker), hits in the calorimetry towers (from ECAL and HCAL), and hits in the muon system. These fundamental inputs are then grouped into "blocks" which the PF algorithm translates into physics objects. Muons are identified by matching a track in the tracker with a hit in the muon system, charged hadrons are identified by matching

a track in the tracker with a hit in HCAL, and electrons are identified by matching a track in the tracker with a hit in ECAL. Photons and neutral hadrons leave no tracks, so they are identified as hits in ECAL and HCAL, respectively, with no matching tracks. As tracks are matched with calorimetry towers and muon hits, those hits are removed from consideration and whichever tower hits are leftover are assumed to be from photons or neutral hadrons. Once all the visible particles are reconstructed, conservation of momentum principles are applied to infer the missing energy, or

The following subsections will detail the methods used to reconstruct each class of particle, and a final subsection will detail the means by which the event data produced by Particle Flow is packaged into formats useful for analysis efforts.

### **3.7.1.1 Track reconstruction and vertexing**

The goal of the silicon tracker is to reconstruct tracks indicating the trajectories of charged particles through the magnetic field, and furthermore to use these trajectories to “trace back” the origin of the particle, known as the vertex. The first vertex in each event, that corresponding to the  $pp$  collision, is known as the primary vertex (PV). The presence of multiple proton-proton collisions in each bunch crossing, a phenomenon known as pileup, presents the possibility of misidentifying the correct PV for a given event. Therefore, there is a need for a vertexing and tracking algorithms exhibiting a high degree of granularity.

To ensure this, tracks with the highest number of hits in the pixel and strip subsystems within the silicon tracker are recorded (and reconstructed) first. Tracks with three hits, high  $p_T$ , and close proximity to the beam spot are considered to be high quality. These tracks are reconstructed first, and their hits removed. For the remaining, lesser-quality tracks, looser criteria are applied iteratively until all tracker hits have been accounted for.

In order to determine the location of the PV, the reconstructed tracks are clustered together and the location is extrapolated by requiring that each track cluster share a plane compatible with the beam line. This is done online as well as offline so that the PV information can be relayed to

the HLT for use in the triggering process. The reconstruction algorithm uses only information from the pixel subdetector for the online reconstruction, while the offline reconstruction uses information from the entire tracker.

### 3.7.1.2 Electron reconstruction

Electrons are reconstructed via the combination of a track in the silicon tracker and hits in the ECAL towers. These tower hits are called “superclusters” and their size in  $\eta$  and  $\phi$  is dictated by various clustering algorithms selected according to the relevant HLT path. As the electron interacts with the silicon in the tracker, it radiates photons via Bremsstrahlung. This emission causes the electron to bend further in the magnetic field. To account for this, the supercluster size is tuned to catch these Bremsstrahlung photons as well, thereby capturing the total energy of the electron before bending and leading to a more accurate calculation of the electron’s energy and momentum.

To fully reconstruct an electron track, one starts with a track **seed**, which is a possible electron trajectory found by interpolating between layer hits in the pixel and strip detectors. These track seeds must be cleaned and filtered in order to find the most likely track candidate, and then they must be matched with a supercluster in ECAL. There are two methods to achieve this. The first, ECAL driven seeding, begins by reconstructing superclusters in ECAL and attempts to match them with track seeds in the innermost layer of the pixel detector. The track is then reconstructed from these track seeds. The second, tracker driven seeding, begins with a high-quality track seed and attempts to match it to an appropriate supercluster in ECAL, while also taking into account other clusters arising from Bremsstrahlung photons. This is achieved by drawing straight lines tangent to the track towards the ECAL. If a corresponding cluster is found, it is added to the total energy of the electron.

### 3.7.1.3 Muon reconstruction

Muons can be measured both in the silicon tracker and the muon system. In order to reconstruct a muon, hits in the muon system (**stand-alone muons**) are matched to hits in the tracker in order to reconstruct a complete muon object, known as a **global muon**. These muons are reconstructed using two different methods, **global muon reconstruction (outside-in)** and **tracker muon reconstruction (inside-out)**.

Global muon reconstruction begins in the muon system. Hits in the DTs and CSCs are allocated into segments, which are short stubs containing just enough hits to assign each a momentum and direction vector. These segments are grouped together to form tracks in the muon system. These tracks, known as stand-alone muon tracks, are matched, one by one, with tracks from the tracker by comparing parameters of the two tracks propagated onto a common surface.

Tracker muon reconstruction begins in the silicon tracker. All tracks with  $p_T > 0.5 \text{ GeV}/c$  and  $p_T > 2.5 \text{ GeV}/c$  are considered possible muon candidates and are propagated outward toward the muon system, taking into account the magnetic field, expected energy loss, and the possibility for multiple Coulomb scattering in the detector material. If a hit in the muon system is found within 3 cm in local  $x, y$  coordinates, the candidate qualifies as a tracker muon.

Tracker muon reconstruction is more efficient than global muon reconstruction at low energies ( $p_T < 5 \text{ GeV}/c$ ), since it only requires one muon segment in the muon system. Global muon reconstruction is more appropriate for muons with higher energies penetrating through more than one station in the muon system.

### 3.7.1.4 Photon and Neutral Hadron Reconstruction

Since photons and neutral hadrons are chargeless, and therefore leave no hits in the silicon tracker, the entirety of their reconstruction takes place in ECAL (photons) and HCAL (hadrons). The identification of photons and neutral hadrons takes place via so-called **clustering algorithms** which are designed to separate photons from neutral as well as charged hadrons, and to differen-

tiate photons originating from the primary or secondary decays from those generated by electrons undergoing Bremsstrahlung within ECAL.

Clustering algorithms involve three steps. First, a seed cluster is identified in one of the ECAL towers as a tower with a local energy maximum passing a threshold specified by the algorithm. Next, topological clusters are defined as clusters adjacent to (sharing at least one side in common with) the seed cluster and with cell energies passing another threshold. These thresholds are generally set to be two standard deviations above the base electronics noise level in each of the separate ECAL segments (80MeV in the barrel and 300MeV in the endcaps). Finally, topological clusters then generate as many “particle flow” clusters as there are seed clusters, and the energy in each particle flow cluster is allocated according to its distance from the seed.

Furthermore, in particle flow, ECAL/HCAL clusters are required **not** to match any tracks in the tracker in order to qualify as photon or neutral hadron candidates.

### 3.7.1.5 Jet Reconstruction

Jets are primarily reconstructed in ECAL and HCAL, although their charged constituents usually leave tracks in the silicon tracker as well. The majority of reconstructed jet energy comes from charged particles such as pions and kaons, and a smaller but still sizable portion comes from photons from  $\pi^0$  decays in ECAL. Though numerous jet reconstruction algorithms exist, most jet candidates are reconstructed using the Particle Flow (PF) algorithm. The PF algorithm looks at the constituent particles in the jet: charged hadrons, neutral hadrons, and photons individually and then clusters them into jet candidates according to various clustering algorithms, the most common of which is the **anti- $k_T$**  algorithm with a cone radius of  $R = 0.5$ . The energy of photons is determined from ECAL measurements, that of charged hadrons is measured with a combination of tracker, ECAL, and HCAL measurements, and the energy of neutral hadrons is measured according to the description in the previous section.

Approximately 90% of the reconstructed jet energy comes from charged hadrons and photons, while the remaining 10% comes from neutral hadrons. Since tracking information from the charged

hadrons is available, improved jet vertexing can be done and the impact of pileup can be mitigated.